

Computational study on the glowing combustion of a wooden ember landing on a non-reacting substrate

Journal of Fire Sciences

1–25

© The Author(s) 2024

Article reuse guidelines:

sagepub.com/journals-permissions

DOI: 10.1177/07349041241256986

journals.sagepub.com/home/jfs

Jiuling Yang^{1,2} , Xiaofeng Peng¹, James Urban^{3,4} , Wei Huang¹, Haoliang Wang¹, Shaojia Wang¹ and Yuqi Hu⁵

Date received: 27 February 2024; accepted: 8 May 2024

Abstract

Despite the increasing frequency in spot ignition by embers in wildfires, research on the multiple physicochemical processes intrinsic to ember combustion is limited. In this study, a two-dimensional computational model was proposed to study the glowing combustion of a wooden ember. A global char oxidation reaction was used to represent the glowing combustion of the ember. A parametric study showed that the porosity, heat of reaction, and oxygen concentration were the most influential parameters on the ember combustion. Then, the model was compared to a series of bench-scale experiments in terms of glowing time and thermal response of a non-reacting substrate when exposed to a hot ember. The simulation results showed that ember combustion was mostly diffusion-controlled rather than kinetic-controlled. Thus, given the ember diversities in spotting fire, modelers should pay more attention to the difference in the physical properties instead of the kinetics between ember species.

Keywords

Spot ignition, glowing combustion, computational model, wooden ember

¹School of Engineering, Sichuan Normal University, Chengdu, P.R. China

²Sichuan Provincial Key Laboratory of Public Fire Prevention and Control Technology, Chengdu, P.R. China

³Department of Fire Protection Engineering, Worcester Polytechnic Institute, MA, USA

⁴Department of Mechanical Engineering, University of California, Berkeley, CA, USA

⁵Sichuan Fire Research Institute of Ministry of Emergency Management of China, Chengdu, P.R. China

Corresponding author:

Yuqi Hu, Sichuan Fire Research Institute of Ministry of Emergency Management of China, Chengdu 610036, P.R. China.

Email: huyuqi@scfri.cn

Introduction

Wildland and Wildland Urban Interface (WUI) fires are the important problems in many areas of the world and may have major consequences in terms of safety, air quality, and damages to buildings, infrastructures, and the ecosystem.¹ The spot fire ignition of a wildland fire by flaming or glowing embers is an important fire ignition pathway by which wildfires and WUI fires occur and propagate.²

Embers refer to any small, hot, carbonaceous particles. Embers differ from hot metal fragments because they are combustible with high carbon fractions. The capability of ember to ignite fuel beds is strongly related to the shape (disk, cylinder, and cube), temperature, and the material type (twig, needle, leaf, etc.), and its combustion regime (flaming or glowing).^{3,4} Cylinder and disk embers are primarily generated from the burning of wildland fuels (grasses, shrubs, and trees) and wooden structures (structural members, shakes, and singles), respectively.² Favored by winds, disk embers are capable of being lofted and migrated over longer distances than the cylinder ones, increasing the capability to ignite fuel beds remotely from fire sources.⁵

A few experiments have been conducted to assess the thermal characteristics and the ignition capability of embers.^{4,6–11} Scott et al.⁷ showed in their experiments that the final burned mass of a single glowing ember increases with the air velocity, and it can cause smoldering ignition in cellulose and sawdust fuel beds. In Woycheese's experiments,¹⁰ it was observed that dense embers quickly self-extinguished with significant residual mass, volume, and density, while for less dense embers, they were likely to burn completely. Fateev et al.'s⁶ experiments showed that an increase in the ember size leads to an increase in smoldering time and a decrease in their mass losses. The tests conducted by Ganteaume et al.⁴ showed that the capability of embers to ignite fuel beds is higher when embers drop in the flaming phase with no air flow, than in the glowing phase with air flow. Recently, Wang et al.⁹ studied the interactions between heterogeneous chemistry and thermomechanical stress of wooden slices under different air velocities and radiant fluxes. They also investigated the size effects on the ignition of wood particles⁸ and further revealed the mechanism of smoldering-to-flaming transition induced by glowing char cracks and cross-wind.¹¹

To better understand the ember ignition mechanism, reliable measurements of the surface temperature of embers are critical. Manzello et al.¹² measured the surface temperature of a single wooden ember exposed to an airflow using an infrared (IR) camera. They found that higher airflow ($1.3\text{--}2.4\text{ m s}^{-1}$) induces a higher surface temperature of the glowing embers. Hakes et al.¹³ and Salehizadeh¹⁴ measured the temperatures in a pile of embers using K-type thermocouples and thin skin calorimeters (TSCs). They recorded higher temperatures at the center of larger ember piles. Tao et al.¹⁵ measured temperatures of the ember pile in three regions, including the upstream, center, and downstream regions of the pile/substrate interface using TSCs. They reported that the peak temperatures were recorded at the center of the pile and that the downstream temperatures were always higher than in the upstream region. Bearinger et al.¹⁶ measured the surface temperature of a single wooden ember to an inert steel plate and found that the peak temperatures ranged from 300°C to 775°C for cylindrical embers and increased to 800°C – 950°C for cuboid embers. To address the limitations of IR thermography associated with its dependency on the emissivity of the ember surface, Urban et al.¹⁷ measured the surface temperature of a single wooden ember using a color pyrometry (CP). The measured mean glowing temperatures ranged from 750°C at 1 m s^{-1} to 950°C at

4 m s^{-1} . It is evident from the above studies that the surface temperature of an ember or ember piles is a transient property that varies spatially and temporally.

The literature temperature measurements summarized above can be used to qualitatively infer how much heat is released by an ember or ember piles. However, it is the heat transfer from the ember to the substrate that determines the ignition propensity of the substrate.¹⁸ A pioneering work by Manzello et al.¹² estimated the heat flux for an ember exposed to an airflow. It was found that the heat flux increased with the airflow velocity (34.2 kW m^{-2} at 2.4 m s^{-1} vs 23.4 kW m^{-2} at 1.3 m s^{-1}). Hakes et al.¹³ measured the heat flux from a single ember and an ember pile by combining a water-cooled heat flux gauge (WC-HFG) with an array of TSCs. They found that the pile mass is critical for ember piles, while ember diameter is more critical for a single ember in terms of the heat transfer to the fuel bed. Salehizadeh¹⁴ extended the work of Hakes et al.¹³ and found that an increase in the ember pile mass increased the peak heat flux from the ember piles. Recent studies by Bearinger et al.¹⁶ and Abul-huda¹⁹ reported high-resolution heat flux measurements from smoldering embers. Abul-Huda et al.¹⁹ developed a spatially resolved optical technique for quantifying the heat flux and the thermal footprint of firebrand piles using laser-induced phosphorescence of YAG: Dy. Bearinger et al.¹⁶ used an IR thermography to quantify the heat flux distributions from an individual ember to a stainless-steel plate. The localized heat flux from a single wooden ember to this inert plate was measured to be $30\text{--}105 \text{ kW m}^{-2}$. Other research works contributed to characterize the generation and transport of firebrand showers.^{5,20–22}

Despite progresses made in experimental studies, the thermochemical effects of ember on spotting ignition have not yet qualitatively and quantitatively been determined. In addition, there is a lack of computational models that can simulate the glowing combustion of a single ember. The major challenge lies in the multiphysics coupling of heat, mass, and momentum transport between porous ember, air flow, and substrate domains. Lautenberger et al.²³ proposed a comprehensive two-dimensional (2D) numerical model to simulate the ignition of a powdered cellulose bed by an ember, from which the ember was treated as a constant volumetric heat source. Thus, it is unlikely to predict the thermochemical effects of embers on the ignition propensity of fuel beds. Warey²⁴ studied the transient heat transfer from an ember to a fuel bed using a zero-dimensional (0D) model for the ember coupled to a transient 2D model for the fuel bed. This model assumed that the transient mass loss (ML) of the ember was only a function of the wind speed, while the effects of the inherent burning dynamics of the ember were not taken into consideration. Lin et al.²⁵ first developed a physics-based 2D computational model to investigate the smoldering ignition of biomass fuel using irradiation spots instead of real embers. This model showed that the minimum irradiation of smoldering ignition increases dramatically as the diameter of the irradiation spots decreases, which helped to understand the spotting fire risk in buildings and wildlands.

The burning temperature and heat flux from a single ember are critical for its glowing combustion and determine the heat transfer to fuel bed. To allow heat fluxes produced by ember to be isolated from igniting the substrate, a 2D computational model with multiphase formulations was proposed and validated to investigate the thermal response (i.e. the glowing temperature and heat flux) of a single ember on a non-reacting sand substrate. The purpose of this model is to solve the coupling of heat, mass, and momentum transport between ember, ambient airflow, and substrate domains, ultimately improving the fundamental understanding of glowing mechanism of embers in wildfires.

Model development

Computational domain

Field experiments conducted in the work by Santamaria et al.²⁶ showed that most of the embers were slices of barks or branches. It is known that the disk-shaped ember is one of the representative embers in wildland and WUI fires,⁵ which is capable of being lofted over a longer distance than embers with the other shapes,⁵ resulting in a greater risk of spotting fire propagation.¹⁰ However, it is impractical to implement simultaneously a cylindrical coordinate system for a disk-shaped ember and a Cartesian coordinate system for a fuel bed within a simulation domain. Thus, for simplicity, a Cartesian coordinate system was used in the whole 2D geometry.

The 2D computational domain is shown in Figure 1, which is consistent with the size of the experimental apparatus used in the work by Scott et al.⁷ Specifically, the wind tunnel test section is 30 cm in length and 8 cm in height. An open boundary Γ_6^{ff} (21 cm along the flow direction) on the ceiling of the wind tunnel is set up for optical access and ember deposition in the experiments. The opening starts 2.86 cm upstream of the edge of the fuel bed. A non-reacting sand bed (15 cm in length \times 5 cm in height) was used as a good surrogate substrate. The top surface of the non-reacting substrate is flush with the floor of the wind tunnel. When depositing on the fuel bed after being combusted, only approximately 20% of the initial mass of the embers remained, with the main component of the residue being char.²⁴ Scanning electron microscope (SEM) analysis results showed that the wooden char presents a fibrous aspect and a porous structure.²⁷ The porous and permeable characteristics of the chars facilitate the penetration of the ambient air toward the center. Thus, it is essential to consider the mass transfer of the airflow inside the ember. Here a small ember with a dimension of 25 mm in diameter and 5 mm in thickness used in the work by Manzello et al.⁵ and Woycheese¹⁰ was used in the simulation. Air velocities of 1, 2, and 3 m s⁻¹ were chosen because they are on the order of buoyancy-induced flow speeds, producing regular flows without overly disturbing the substrate surface.⁷

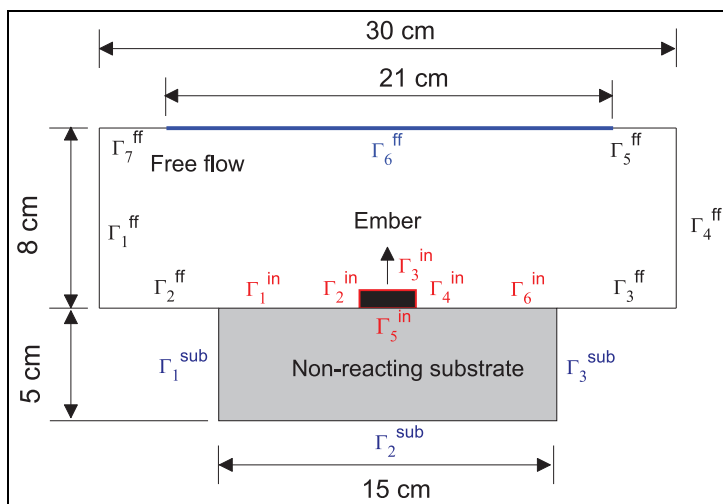


Figure 1. Illustration of the proposed 2D computational domain.

Ember combustion model

It is known that embers are most likely in a state of glowing combustion when landing on the fuel beds.⁵ Here the glowing combustion of an ember is represented using a global one-step char oxidation reaction (equation (1)).²⁸



In the process of a combustion reaction, the ember surface temperature can reach more than 900°C in the first few seconds before falling below a lower temperature.⁶ Therefore, the ember combustion is neither perfectly diffusion- nor kinetic-controlled. The char surface oxidation processes occur in series as first diffusion of oxygen and then kinetic consuming that oxygen. The leading cause for the differences between these two regimes mainly stems from the competition between the chemical reaction rate and the mass transfer rate. The burning temperature and airflow velocity affect the competition relationship.²⁹ Char oxidation proceeds as a circuit in which the oxygen flows through the kinetic and diffusion resistances.³⁰ The overall glowing combustion rate of an ember is calculated using equation (2).³⁰

$$\dot{\omega}_{co}''' = \frac{1}{\left(\dot{\omega}_{co}'''|_{diff}\right)^{-1} + \left(\dot{\omega}_{co}'''|_{kin}\right)^{-1}} \quad (2)$$

Here $\dot{\omega}_{co}'''|_{diff}$ and $\dot{\omega}_{co}'''|_{kin}$ are the ember combustion rate controlled by diffusion and kinetics, respectively.

Diffusion-controlled ember combustion. If the ember combustion is only diffusion-controlled, the glowing combustion rate is determined by the oxygen transferred to the char surface from the pores (equation (3)). The mass fraction of oxygen on the char surface y_{s, O_2} can be assumed to be zero.³⁰

$$\dot{\omega}_{co}'''|_{diff} = \frac{1}{\nu_{O_2, co}} \rho_g (y_{b, O_2} - y_{s, O_2}) S_v h_m \quad (3)$$

Where $\nu_{O_2, co}$ is the mass consumption coefficient of oxygen (see equation (1)), y_{b, O_2} is the mass fraction of oxygen in the pores, S_v (m^{-1}) is the internal surface area per unit volume, h_m ($m s^{-1}$) is the mass transfer coefficient. To calculate the mass transfer coefficient h_m , correlation for the Sherwood number (Sh: dimensionless mass transfer coefficient)³¹ is used as follows

$$Sh = \frac{h_m d_p}{D} = 2 + 0.81(\varphi_{em})^{-1/2} (Re_p)^{1/2} (Sc)^{1/3}, 0 < Re_p < 500 \quad (4)$$

The particle Reynolds number¹⁹ is given by

$$Re_p = \frac{\|\mathbf{u}_p\| d_p}{\nu} \quad (5)$$

The Schmidt number (Sc) is given by

$$Sc = \frac{\nu}{D} \quad (6)$$

The ember is modeled as a porous matrix with pore diameters, d_p . $\|\mathbf{u}_p\|$ is the local porous flow velocity inside the porous pores, ν is the kinematic viscosity of a gas mixture, and D is the gas diffusion coefficient.

Kinetic-controlled ember combustion. If the ember combustion is only kinetic-controlled, for simplicity, it assumes that the ember has only one component of char and no ash is formed after glowing ($m_a = 0$, because the ash density is negligible compared to the char density²⁴ and ash is blown away by wind). Thus, the completely burned ember zone will turn to be airflow-free zone. The mass conversion of the ember is expressed as equation (7)

$$\alpha = 1 - \frac{m - m_a}{m_0 - m_a} = 1 - \frac{m}{m_0} \quad (7)$$

where m and m_0 refer to the real-time mass and the initial mass of the ember, respectively. The mass fraction of ember is $y_c = m/m_0 = 1 - \alpha$. It assumes that there is no volume change of the ember during the glowing combustion process.

The power-law model is proved to describe the combustion kinetics of a wooden char accurately.³² The glowing combustion rate of an ember (equation (8)) is expressed by the Arrhenius law, which is a function of the oxygen concentration and the mass fraction of the char y_c

$$\dot{m}_{co}'''|_{kin} = -\rho_{em,0} A_c \exp\left(-\frac{E_c}{RT_{em}}\right) (y_c)^{n_c} \left(\frac{x_{b,O_2}}{0.205}\right)^{n_{O_2}} \quad (8)$$

where $\rho_{em,0}$ is the initial bulk density of an ember, A_c and E_c are the pre-exponential factor (s^{-1}) and activation energy ($kJ\ mol^{-1}$), respectively. n_c and n_{O_2} are the reaction orders, x_{b,O_2} is the volume fraction of the oxygen in pores that equals to

$$x_{b,O_2} = y_{b,O_2} M_{air} / M_{O_2} \quad (9)$$

where M_{air} and M_{O_2} are the molecular mass ($g\ mol^{-1}$) of the air and the oxygen, respectively.

Here a base case is first chosen to investigate the basic glowing mechanism of a wooden ember, that is, Char-TGA.³³ The kinetic parameters of Char-TGA can be found in Table 1. The material properties used in the base case are mainly from literature experiments (see Table 2). Determining the thermal conductivity of a wooden ember is challenging due to its dependency on the pyrolysis conditions. Janssens's³⁷ approximate calculation can help determine the conductivity of embers as a function of density and temperature (equations (10))

Table 1. Kinetic parameters of the wooden char as a surrogate for the wooden ember.

Char type	$\log A_c(\log s^{-1})$	$E_c(kJ\ mol^{-1})$	$n_c(-)$	$n_{c,O_2}(-)$	$\Delta H_c(MJ\ kg^{-1})$	Ref.
Char-TGA	6.55	124.0	0.56	0.68	-17.4 ^a	Anca-Couce et al. ³³

Table 2. Material properties of the ember.

Cases	ρ_{em} (kg m ⁻³)	λ_{em} (W m ⁻¹ K ⁻¹)	c_{em} (J kg ⁻¹ K ⁻¹)	φ_{em} (-)	$K_{em} \times 10^{-9}$ (m ²)	ε_{em} (-)
Base case	127.39 ^{a 34}	Equations (10)–(11)	Equation (12)	0.95 ^{b 23}	2.5 ³⁵	0.6 ¹²
Typical range	[43.50, 178.35] ¹⁰	[0.25 λ_{em} , 1.25 λ_{em}]	[0.25 c_{em} , 1.25 c_{em}]	[0.80, 0.98] ³⁶	[0.1, 10] ³⁵	[0.4, 0.8] ³⁶

^aCalculated from the mass and the volume of a single glowing ember in the work by Manzello et al.³⁴

^bCalculated by $\varphi_{em} = 1 - 0.2(1 - \varphi_{wood})$, only 20% of the initial mass remained when the wooden ember deposits on the fuel bed,²⁴ the porosity of the virgin white pine wood (φ_{wood}) is 0.757.³⁵

Table 3. Material properties of the “ideal” non-reacting porous substrate.⁴⁰

Material	ρ_{sub} (kg m ⁻³)	λ_{sub} (W m ⁻¹ K ⁻¹)	c_{sub} (J kg ⁻¹ K ⁻¹)	φ_{sub} (-)	$K_{sub} \times 10^{-9}$ (m ²)	ε_{sub} (-)
Ideal substrate	420	0.24	230	0.82	3.66	0.9

and (11)). The specific heat capacity of an ember (c_{em}) varies little among wood embers and thus c_{em} is regarded as a function of only temperature³⁸ (equation (12)).

$$\lambda_{wood} = 0.00249 + 0.000145 \times \rho_{wood} + 0.000184 \times (T_{wood} - 273) \quad (10)$$

$$\lambda_{em} / \lambda_{wood} \approx \rho_{em} / \rho_{wood} = 0.25 \quad (11)$$

$$c_{em} = 714 + 2.34 \times (T_{em} - T_0) - 0.000834 \times (T_{em} - T_0)^2 - 3.67 \cdot 10^{-7} \times (T_{em} - T_0)^3 \quad (12)$$

It is useful to investigate the heat flux generated by an ember landing on a non-reacting substrate instead of a combustible fuel bed²⁶ because the fuel decomposition in turn brings reaction heat to the ember. It assumes that the non-reacting substrate has similar material properties as a porous cellulose fuel bed in the work by Lautenberger and Fernandez-Pello,²³ and Urban et al.,³⁹ that is, an “ideal” non-reacting porous substrate (see Table 3).

Governing equations

Heat transfer field. In this model, local thermal equilibrium is implemented in the porous ember and the non-reacting substrate. The heat transfer equations in the free flow (T_{ff}), porous ember (T_{em}), and non-reacting substrate (T_{sub}) are expressed as equations (13)–(15), respectively.

$$\rho_g c_g \partial T_{ff} / \partial t + \rho_g c_g \mathbf{u}_f \cdot \nabla T_{ff} = \nabla \cdot (\lambda_g \nabla T_{ff}) \quad (13)$$

$$(\rho c)_{em, eff} \partial T_{em} / \partial t + \rho_g c_g \mathbf{u}_p \cdot \nabla T_{em} = \nabla \cdot (\lambda_{em, eff} \nabla T_{em}) + \omega'''_{co} \Delta H_c \quad (14)$$

$$(\rho c)_{sub, eff} \partial T_{sub} / \partial t + \rho_g c_g \mathbf{u}_p \cdot \nabla T_{sub} = \nabla \cdot (\lambda_{sub, eff} \nabla T_{sub}) \quad (15)$$

The laminar flow velocity vector \mathbf{u}_f in equation (13) is deduced from Navier–Stokes equations, while the \mathbf{u}_p in equations (14) and (15) is invoked ($\mathbf{u}_p = \phi \mathbf{u}_f$) by Brinkman equations. The heat transfer in the porous ember (equation (14)) and the non-reacting substrate (equation (15)) involves the interactions of solid and gas mixture. Thus, the effective volumetric heat capacity and the thermal conductivity of the ember are $(\rho c)_{em,eff} = \phi_{em} \rho_g c_g + (1 - \phi_{em}) \rho_{s,em} c_{em}$ and $\lambda_{em,eff} = \phi_{em} \lambda_g + (1 - \phi_{em}) \lambda_{em,s} + 16 \cdot \sigma d_p T_{em}^3 / 3$, respectively. Similarly, the effective volumetric heat capacity and the thermal conductivity of the non-reacting substrate are $(\rho c)_{sub,eff} = \phi_{sub} \rho_g c_g + (1 - \phi_{sub}) \rho_{s,sub} c_{sub}$ and $\lambda_{sub,eff} = \phi_{sub} \lambda_g + (1 - \phi_{sub}) \lambda_{sub,s}$, respectively.

Gas flow field. The compressible laminar flow in the free flow is governed by the Navier–Stokes equation (equation (16)), while the porous flow in the ember (equation (17)) and the substrate (equation (18)) is described by the Brinkman equation that extends the Darcy’s law to consider the dissipation of the kinetic energy by viscous shear. The volume force \mathbf{F} is expressed as the gravity force $\mathbf{F} = \rho_g \mathbf{g}$. The mass continuity equations of a gas mixture are expressed as equations (19)–(21), for the free flow, porous ember, and the non-reacting substrate, respectively.

$$\rho_g \partial \mathbf{u}_f / \partial t + \rho_g (\mathbf{u}_f \cdot \nabla) \mathbf{u}_f = \nabla \cdot [-p_f \mathbf{I} + \mu (\nabla \mathbf{u}_f + (\nabla \mathbf{u}_f)^T) - 2\mu (\nabla \cdot \mathbf{u}_f) \mathbf{I}] + \mathbf{F} \quad (16)$$

$$\begin{aligned} \frac{\rho_g}{\phi_{em}} \left(\frac{\partial \mathbf{u}_p}{\partial t} + (\mathbf{u}_p \cdot \nabla) \frac{\mathbf{u}_p}{\phi_{em}} \right) = \nabla \cdot \left[-p_p \mathbf{I} + \frac{\mu}{\phi_{em}} (\nabla \mathbf{u}_p + (\nabla \mathbf{u}_p)^T) - \frac{2\mu}{3\phi_{em}} (\nabla \cdot \mathbf{u}_p) \mathbf{I} \right] \\ \left(-\frac{\mu}{K_{em}} + \frac{\dot{m}_{em}^m}{\phi_{em}} \right) \mathbf{u}_p + \mathbf{F} \end{aligned} \quad (17)$$

$$\begin{aligned} \frac{\rho_g}{\phi_{sub}} \left(\frac{\partial \mathbf{u}_p}{\partial t} + (\mathbf{u}_p \cdot \nabla) \frac{\mathbf{u}_p}{\phi_{sub}} \right) = \nabla \cdot \left[-p_p \mathbf{I} + \frac{\mu}{\phi_{sub}} (\nabla \mathbf{u}_p + (\nabla \mathbf{u}_p)^T) - \frac{2\mu}{3\phi_{sub}} (\nabla \cdot \mathbf{u}_p) \mathbf{I} \right] \\ - \frac{\mu}{K_{sub}} \mathbf{u}_p + \mathbf{F} \end{aligned} \quad (18)$$

$$\partial \rho_g / \partial t + \nabla \cdot (\rho_g \mathbf{u}_f) = 0 \quad (19)$$

$$\partial (\phi_{em} \rho_g) / \partial t + \nabla \cdot (\rho_g \mathbf{u}_p) = \omega_{co}''' \quad (20)$$

$$\partial (\phi_{sub} \rho_g) / \partial t + \nabla \cdot (\rho_g \mathbf{u}_p) = 0 \quad (21)$$

Mass transfer field. The mass transport in multicomponent system is controlled by the mixture composition, temperature, and pressure. The mass conservation equations for gas species in the free flow, porous ember, and the non-reacting substrate are expressed as equations (22)–(24), respectively. Here \mathbf{j}_j is the diffusion model expressed by the Fick’s law

$\mathbf{j}_j = - \left(\rho_g D_j \nabla y_j + \rho_g y_j D_j \frac{\nabla M_n}{M_n} \right)$, ρ_g is the gas mixture density defined by the ideal gas law $\rho_g = \frac{p M_n}{R T_g}$, M_n is the mean molar mass expressed as $M_n = \left(\sum_j \frac{y_j}{M_j} \right)^{-1}$. Three gas-phase species of O_2 , N_2 , and CO_2 are considered. The effective diffusivity in the porous medium is

expressed by the Bruggeman model $D_{pm,j} = \varphi_{pm}^{3/2} D_{ff,j}$, which is related to the free-flow diffusivity $D_{ff,j}$.

$$\rho_g \partial y_{ff,j} / \partial t + \nabla \cdot \mathbf{j}_{ff,j} + \rho_g (\mathbf{u}_f \cdot \nabla) y_{ff,j} = 0 \quad (22)$$

$$\rho_g \partial y_{em,j} / \partial t + \nabla \cdot \mathbf{j}_{em,j} + \rho_g (\mathbf{u}_p \cdot \nabla) y_{em,j} = R_{em,j} \quad (23)$$

$$\rho_g \partial y_{sub,j} / \partial t + \nabla \cdot \mathbf{j}_{sub,j} + \rho_g (\mathbf{u}_p \cdot \nabla) y_{sub,j} = 0 \quad (24)$$

Here, no gas-phase reactions in the whole domain are assumed. The mass transport of a gas species is only driven by convection and diffusion. In the free flow and non-reacting substrate, the reaction rates $R_{em,j}$ of O_2 , N_2 , and CO_2 are zero, while in the porous ember, they are $-\nu_{O_2, co} \omega_{co}'''$, 0, and $(1 + \nu_{O_2, co}) \omega_{co}'''$, respectively.

It is noted that the ember is modeled as a kind of a porous fuel. The porous structure is manifested through two parameters of the porosity and the permeability in the energy balance (equation (14)) and the Brinkman equations (equation (17)), respectively. Thus, the heat and mass transfer inside the porous ember can be modeled. In addition, the internal surface area per unit volume S_v and mass transfer coefficient h_m in equation (3) are associated with the porous structure through the particle and the pore diameters of the ember.

Boundary and initial conditions. The boundary and initial conditions are listed in Tables 4 and 5, respectively. A single-domain approach is applied in the temperature, gas flow, and mass transfer fields. Thus, no matching conditions at the internal interfaces of $\Gamma_1^{\text{in}} - \Gamma_6^{\text{in}}$ are needed for the gas flow and the mass transfer fields. On the external walls of $\Gamma_{2,3,5,7}^{\text{ff}}$ and $\Gamma_{1,2,3}^{\text{sub}}$, no gas flow or heat penetration occurs across the boundaries.

For the calculation of the radiative flux at $\Gamma_2^{\text{in}} - \Gamma_4^{\text{in}}$, these boundaries are assumed as opaque diffuse surfaces and ideal gray bodies which reflect radiative intensity uniformly in all directions. The net radiative heat flux at $\Gamma_2^{\text{in}} - \Gamma_4^{\text{in}}$ is given by equation (25).

$$-\mathbf{n} \cdot \mathbf{q}|_{\Gamma_2^{\text{in}} - \Gamma_4^{\text{in}}} = \varepsilon_{em} (T_0^4 - T_{em}^4) \quad (25)$$

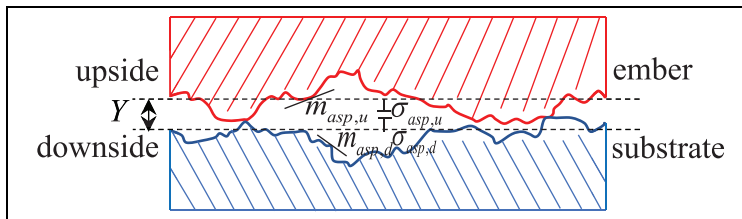
Solid surfaces comprised peaks and valleys of varying size and shape, and this unevenness is the basic cause of the thermal contact resistance between ember and substrate. The thermal contact resistance is highly dependent of material properties, for example, surface roughness, gas gap, and so on. The estimation of the thermal contact resistance plays a vital role in precisely evaluating the heat transfer from ember to substrate. Especially for looser substrate (e.g., pine needle bed and wood chips), the influences of the thermal contact resistance are particularly significant because of the poor contact with ember due to its higher porosity and permeability. At the interface Γ_5^{in} of the ember and the substrate in contact, a scenario of poor contact with the substrate was investigated (see Figure 2). The thermal contact resistance is calculated by a model proposed by in the work by Yovanovich.⁴¹ The joint conductance h is involved in the heat flux across the interface Γ_5^{in} (equations (26)–(31)), which comprised three components: constriction conductance h_c (from the contact spots), gap conductance h_g (due to air at the interstitial space), and radiative conductance h_r . θ_{asp} , δ_{asp} , H_c , p , Y_{gap} , M_{gap} , and ε are asperities average slope, asperities average height, micro-hardness, contact pressure, mean separation thickness, and the emissivity, respectively. The subscripts “ u ” and “ d ” represent the upside and downside at interface, corresponding to the

Table 4. Boundary conditions used in this model.

Domains	Boundaries	Heat transfer	Gas flow	Mass transfer
Free flow	$\Gamma_1^{ff}(\text{inlet})$	$T_{ff} = T_0$	$u_x = u_0$	$y_{O_2} = 0.23, y_{N_2} = 0.77$
	$\Gamma_2^{ff} \Gamma_3^{ff} \Gamma_5^{ff} \Gamma_7^{ff}(\text{walls})$	$-\mathbf{n} \cdot \mathbf{q} = 0$	$u_y = 0$	$y_{CO_2} = 0$
	$\Gamma_6^{ff}(\text{open boundary})$	$T_{ff} = T_0$ if $\mathbf{n} \cdot \mathbf{u}_f \geq 0$ $-\mathbf{n} \cdot \mathbf{q} = 0$	$\mathbf{u}_f \cdot \mathbf{n} = 0$ $-\mathbf{p}_f \mathbf{l} +$ $\mu(\nabla \mathbf{u}_f + (\nabla \mathbf{u}_f)^T)$ $-2\mu(\nabla \cdot \mathbf{u}_f)\mathbf{l}/3 = 0$	$-\mathbf{n} \cdot (\mathbf{j}_j + \rho_g \mathbf{u}_f y_{ff,j}) = 0$ if $\mathbf{n} \cdot \mathbf{u}_f \geq 0$ $-\mathbf{n} \cdot \rho_g D_{ff,j} \nabla y_{ff,j} = 0,$ if $\mathbf{n} \cdot \mathbf{u}_f < 0$
	$\Gamma_4^{ff}(\text{outlet})$	$-\mathbf{n} \cdot \mathbf{q} = 0$	$p_{ff} = p_0$	$y_{ff,j} = y_{ff,j} _{\infty}$ $-\mathbf{n} \cdot \rho_g D_{ff,j} \nabla y_{ff,j} = 0$
Ember	$\Gamma_2^{in} \Gamma_3^{in} \Gamma_4^{in}(\text{surfaces})$	$-\mathbf{n} \cdot \mathbf{q}$ $= \varepsilon_{em}(T_0^4 - T_{em}^4)$	—	—
	$\Gamma_5^{in}(\text{interface})$	$-\mathbf{n} \cdot \mathbf{q} = -h\Delta T$	—	—
Non-reacting substrate	$\Gamma_1^{in} \Gamma_6^{in}(\text{surfaces})$	—	—	—
	$\Gamma_1^{sub} \Gamma_2^{sub} \Gamma_3^{sub}(\text{walls})$	$-\mathbf{n} \cdot \mathbf{q} = 0$	$\mathbf{u}_p \cdot \mathbf{n} = 0$	$-\mathbf{n} \cdot (\mathbf{j}_j + \rho_g \mathbf{u}_p y_{sub,j}) = 0$

Table 5. Initial conditions used in this model.

Domains	Temperature	Gas velocity	Mass fractions
Free flow	$T_{ff} = T_0$	$\mathbf{u}_f = 0$ m/s	$y_{O_2} = 0.23, y_{N_2} = 0.77, y_{CO_2} = 0$
Ember	$T_{em} = T_{em,0} = 900$ °C	$\mathbf{u}_p = 0$ m/s	$y_{O_2} = 0.23, y_{N_2} = 0.77, y_{CO_2} = 0, y_c = 1$
Non-reacting substrate	$T_{sub} = T_0$	$\mathbf{u}_p = 0$ m/s	$y_{O_2} = 0.23, y_{N_2} = 0.77, y_{CO_2} = 0$

**Figure 2.** Sketch of a likely scenario of poor contact between an ember and a substrate at the microscopic level.

ember bottom and the substrate surface, respectively. The main model inputs involved in this boundary condition are given in Table S1 in the Supplementary Materials. More information about the thermal boundary condition can be found in the work by Warey.²⁴

$$-\mathbf{n}_u \cdot (-\lambda_u \nabla T_u) = -h(T_d - T_u) \quad (26)$$

$$-\mathbf{n}_d \cdot (-\lambda_d \nabla T_d) = -h(T_u - T_d) \quad (27)$$

$$h = h_c + h_g + h_r \quad (28)$$

$$h_c = 1.25 \left(\frac{2\lambda_u \lambda_d}{\lambda_u + \lambda_d} \right) \left(\frac{\theta_{asp}}{\delta_{asp}} \right) \left(\frac{p}{H} \right)^{0.95} \quad (29)$$

$$h_g = \frac{\lambda_g}{Y + M_g} \quad (30)$$

$$h_r = \frac{\varepsilon_u \varepsilon_d}{\varepsilon_u + \varepsilon_d - \varepsilon_u \varepsilon_d} \sigma (T_u^3 + T_u^2 T_d + T_u T_d^2 + T_d^3) \quad (31)$$

For the base case, the initial ember temperature is 900°C, imitating the initial state of glowing ember when it lands on the substrate. The glowing ignition will be triggered by its high initial temperature. The ember will immediately cool down once it lands on the substrate due to the blowing effects of airflow. In the model, it is challenging to capture the initial temperature variation of ember at the moment when it lands on the substrate. Hence, the ignition protocol used in the model is not completely representative of the actual experiments and spotting ignition.

The partial differential equations (PDEs) (equations (13)–(24)) are first discretized into discrete equations, along with the initial and boundary conditions (see Table 4 and Table 5), the closed equation system is then numerically computed using a Finite Element Method (FEM) code pack in COMSOL Multiphysics 6.0. The whole domain was meshed by 29,312 free triangles and 756 boundary elements. The mesh inside the ember and around the ember exterior (~ 1 cm away) were refined to converge well. The rectangular corners of ember were tailored to be fillets (the vertices radius is 0.25 cm) to avoid numerical singularity. The time steps were chosen dynamically to ensure stability and accuracy in the solution, ranging from 0.001 at the beginning to a maximum step of 0.05 s. Increasing the total grid number and decreasing the maximum time step by a factor of 2, resulted in less than 1% variation of the ML of an ember after 600 s but cost more than triple computing time. The computation of the base case required about 12 h of CPU time on a 11th Gen Intel Core i7-11700® 2.5 GHz eight-core computer.

Results and discussions

Basic glowing behavior

As seen in Figure 3(a) ($u_0 = 0.5 \text{ m s}^{-1}$, $T_{\text{em}, 0} = 900^\circ\text{C}$), the leading edge (upwind region) of the ember exhibits a high-glowing combustion temperature ($> 900^\circ\text{C}$) while the trailing edge (downwind region) presents a low temperature ($< 500^\circ\text{C}$). As seen in Figure 3(b), the temperature distributes non-uniformly along the ember bottom line (x -axis ranges from 13.75 to 16.25 cm). The peak temperature at the ember bottom line increases from approximately 660°C at 100 s to 800°C at 300 s.

The glowing combustion of an ember is a multidimensional phenomenon. The progression rate difference between the top and lower portions of the ember, and the competition between the oxygen supply and the heat loss determine the glowing structure. As seen from Figure 4(a), a curved char oxidation frontline, that is, glowing frontline, forms in the ember

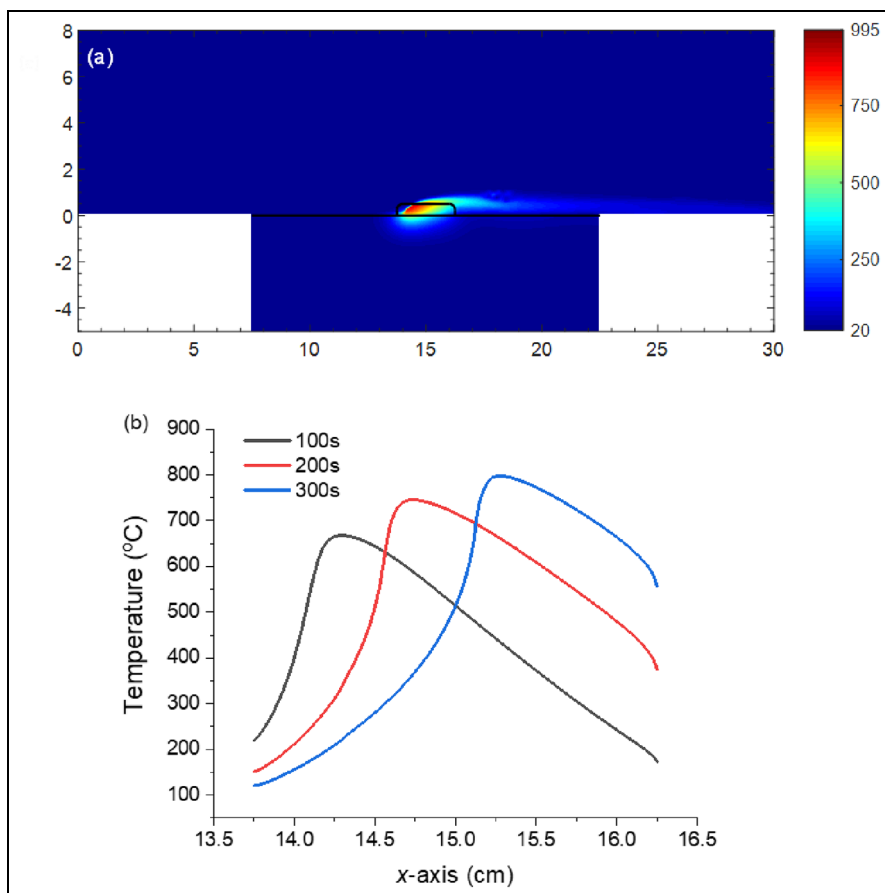


Figure 3. (a) Temperature map (°C) in the whole computational domain at $t = 100$ s, and (b) temperature profiles (°C) at $t = 100, 200$, and 300 s along the ember bottom line. Base case: $u_0 = 0.5 \text{ m s}^{-1}$, $T_{\text{em},0} = 900^\circ\text{C}$.

at $t = 100$ s. The frontline moves forward to the right with an increased arc length at $t = 200$ s (Figure 4(b)). After 300 s (Figure 4(c)), the glowing frontline further spreads to the lower right corner of the ember with a decreased glowing combustion rate. The glowing combustion rate of the ember slows down as the char oxidation frontline approaching the free ember surface due to large heat losses to the environment. In contrast, the spread rate driven by local burning rate decreases from the top surface to the ember bottom. The glowing frontline spreads faster in the free ember surface due to sufficient oxygen supply. The long-arc glowing structure is different from the 2D overhang structure of smoldering peat with a multi-reaction scheme,^{42,43} in which smoldering spreads faster beneath the free surface. This 2D glowing structure of the ember indicates that 0D or 1D models may fail to reveal its real glowing behavior under wind conditions.

Figure 5(a) shows the normalized ML (–) and mass loss rate (MLR, s^{-1}) of the ember. Generally, the glowing combustion of the ember can be divided into three stages. At Stage I,

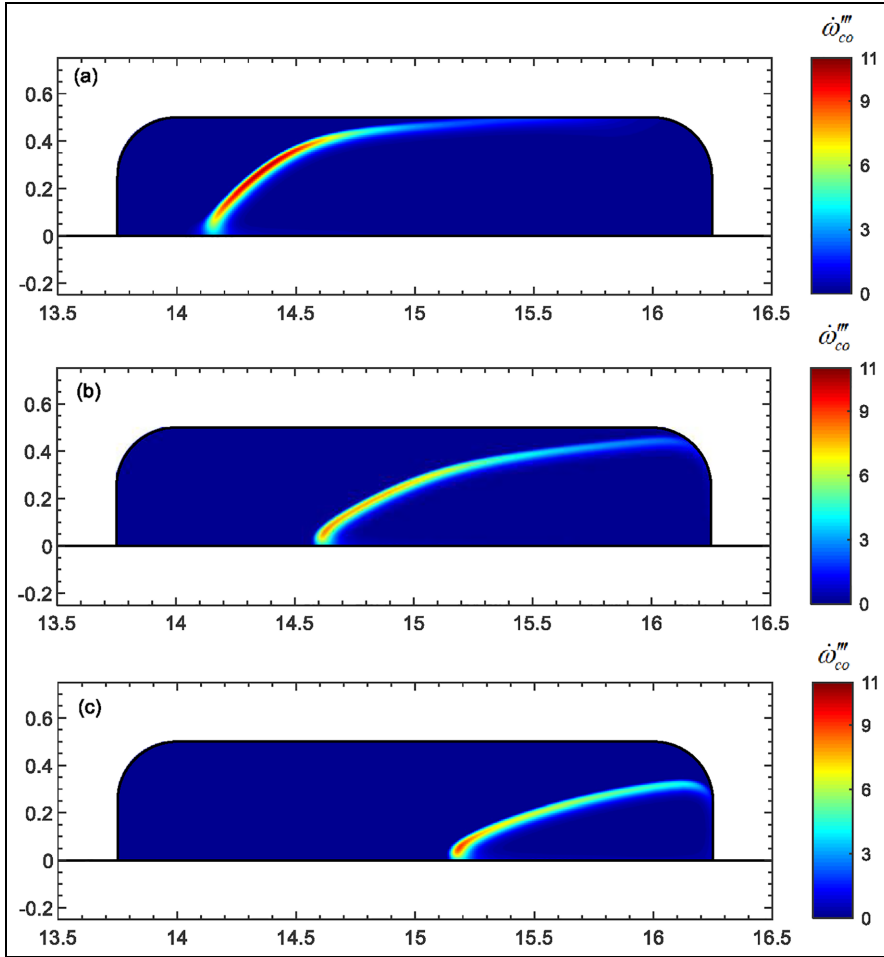


Figure 4. Glowing combustion rate of ember $\dot{\omega}_{co}'''$ ($\text{kg m}^{-3} \text{s}^{-1}$) at (a) $t = 100$ s, (b) $t = 200$ s, and (c) $t = 300$ s. Base case: $u_0 = 0.5 \text{ m s}^{-1}$, $T_{\text{em},0} = 900^\circ\text{C}$.

a sharp drop in MLR with a small shoulder within the first 50 s is identified, corresponding to a monotonically decreasing transient average heat flux $Q_c''|_{\Gamma_{\text{in}}}$ through the ember bottom (see Figure 5(b)). Subsequently, a stable Stage II (50–120 s) is observed for MLR and $Q_c''|_{\Gamma_{\text{in}}}$. The transient average heat flux at this stage is about 17.5 kW m^{-2} , which is comparable to the average heat flux of a single ember in Hakes' measurements.¹¹ Finally, the MLR and $Q_c''|_{\Gamma_{\text{in}}}$ gradually decays (Stage III (120–437.3 s)).

After 437.3 s, the ember ceases glowing combustion without losing mass. Thus, the lifetime of the ember (LTE) is 437.3 s in the base case. In the LTE, the total energy per unit area through the ember bottom $(Q_{\text{all}}'''|_{\Gamma_{\text{in}}} = \int_0^{\text{LTE}} Q_c''|_{\Gamma_{\text{in}}} dt)$, that is, the integrated transient average heat flux in time, is about 5700 kJ m^{-2} . The simulated results showed that the effects of thermal contact resistance between the ember and sand are negligible (see Figure S5 in the Supplementary Materials). Without considering the contact resistance, the glowing

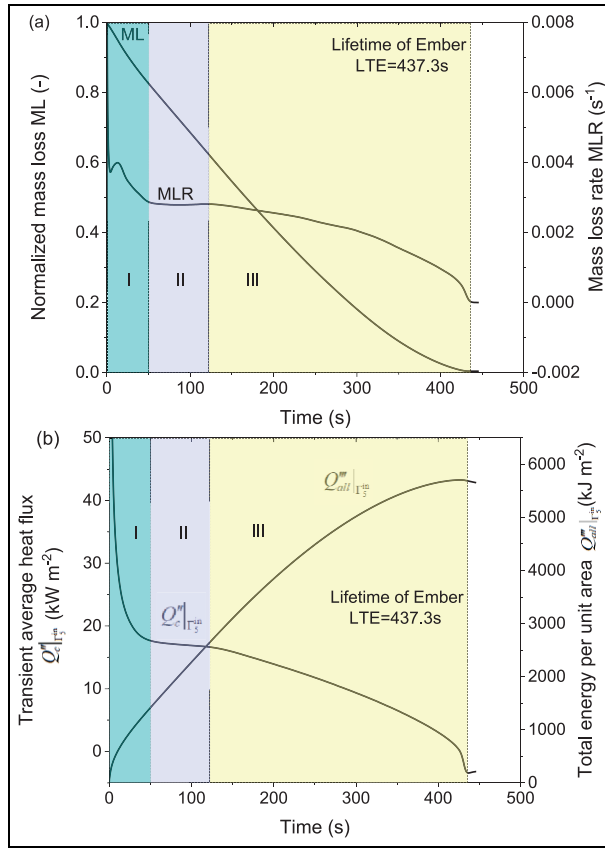


Figure 5. (a) Normalized ML (—) and MLR (s⁻¹) of the ember, and (b) transient average heat flux $Q_c''|_{\Gamma_s}$ (kW m⁻²) and total energy per unit area $Q_{all}'''|_{\Gamma_s} = \int_0^{LTE} Q_c''|_{\Gamma_s} dt$ (kJ m⁻²) through the ember bottom.

combustion of ember ceases at 430 s, earlier than that (438 s) (Figure S5(a)) when considering contact resistance; the total energy per unit area is 5830 kJ m⁻², which is slightly higher than that (5700 kJ m⁻²) when considering contact resistance (Figure S5(b)).

Two regimes of glowing combustion, namely, kinetic- and diffusion-controlled, are distinguished depending on the ember temperature (see Figure 6(a)). The hot ember exhibits a similar temperature variation to a non-reacting metal particle.⁴⁴ The temperature at the ember center first undergoes an initial significant drop (from 900°C to 500°C) but quickly turns to an increment in Figure 6(a). At initial stage (0–100 s) in Figure 6(b), the kinetic-controlled char oxidation rate is close to the overall char oxidation rate ($\dot{\omega}_{co}'''|_{kin} \approx \dot{\omega}_{co}'''$), but is smaller than a 10th of the diffusion-controlled char oxidation rate ($\dot{\omega}_{co}'''|_{kin} < \dot{\omega}_{co}'''|_{diff}/10$). It means that the glowing combustion of the ember is kinetic-controlled at low temperature (< 650°C). At the intensive glowing stage (150–220 s, see Figure 6(a)), the diffusion-controlled char oxidation rate is close to the overall char oxidation rate ($\dot{\omega}_{co}'''|_{diff} \approx \dot{\omega}_{co}'''$) but

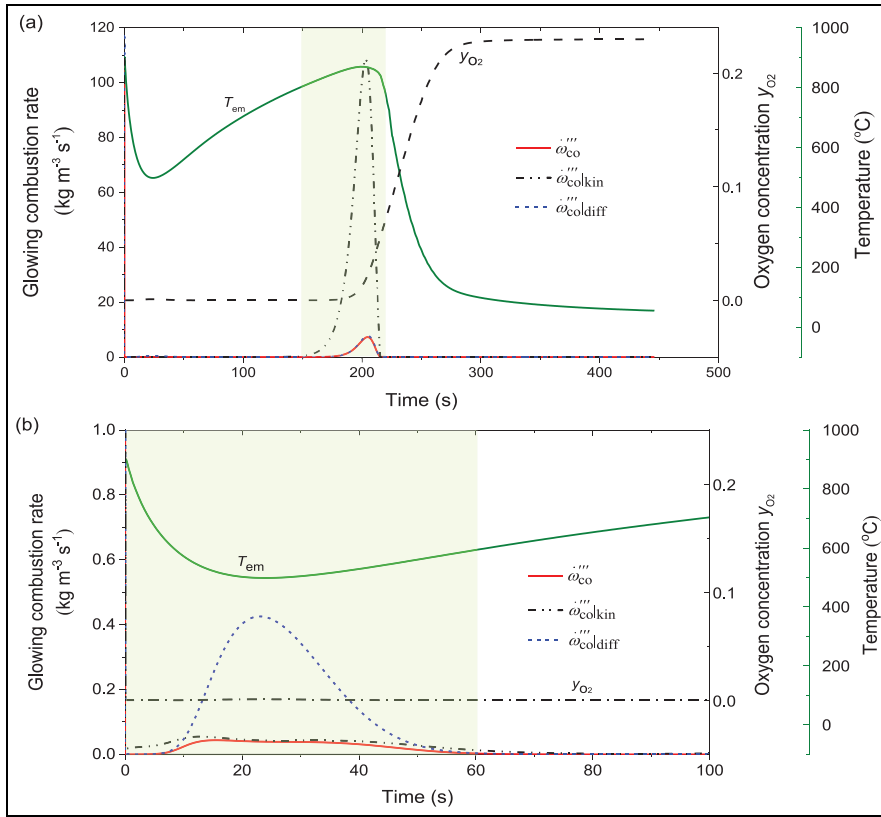


Figure 6. (a) Simulated glowing combustion rate, oxygen concentration, and temperature at the ember center; (b) zoom-in graph from 0 to 100 s of Figure 6(a), the glowing combustion rate ranges from 0 to 1.

is smaller than a 10th of the kinetic-controlled char oxidation rate $\left(\dot{\omega}_{co}'''|_{diff} < \dot{\omega}_{co}'''|_{kin}/10\right)$. It means that the glowing combustion of ember is diffusion-controlled at relatively high temperature ($> 700^{\circ}\text{C}$), which depends on the oxygen supplied to the char surface.

Parametric study

As reported in the literature, the material properties and chemical kinetics of a wooden ember may vary significantly. Thus, a parametric study is conducted to investigate the performance of these parameters affecting the glowing characteristics of the ember. The upper and lower limits of the specific heat capacity and thermal conductivity of the non-reacting substrate are unavailable from literature. Thus, the effects of material properties of substrate on the glowing combustion of ember are out of the scope of this article.

First, the one-at-a-time sensitivity analysis⁴⁵ (only one parameter varies at a time while holding all the others as the base case values) is studied. Next, a differential sensitivity analysis⁴⁵ is performed to quantify the effects of the material properties. Here three candidates of y_1 , y_2 , and y_3 are selected as the dependent variable y , which represents the LTE, the total

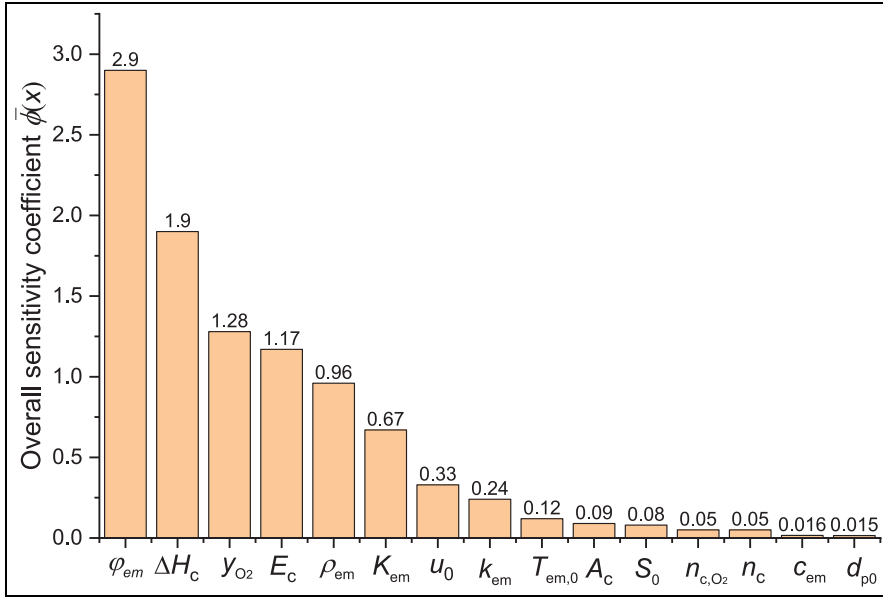


Figure 7. The overall sensitivity coefficient $\bar{\phi}(x)$ of main model inputs.

ML at the LTE, and the peak energy per unit area through the ember bottom $Max - Q''_{all}|_{\Gamma_5^{in}}$ ($Q''_{all}|_{\Gamma_5^{in}} = \int_0^{LTE} Q''_c|_{\Gamma_5^{in}} dt$), respectively. Here $Q''_c|_{\Gamma_5^{in}}$ is the transient average heat flux at the interface (Γ_5^{in}) between the ember and the substrate. For each candidate y_i , the sensitivity to the independent variable x is calculated by equation (32). The upper (x_{up}) and lower (x_{low}) limits can be found in Table 2. The overall sensitivity of x is measured by a weighted sensitivity coefficient (equation (33))

$$\phi_i(x) = \sqrt{\left(\frac{|y_i(x_{up}) - y_i(x_0)|}{(x_{up} - x_0)} \cdot \frac{x_0}{y_i(x_0)} \right)^2 + \left(\frac{|y_i(x_{low}) - y_i(x_0)|}{|x_{low} - x_0|} \cdot \frac{x_0}{y_i(x_0)} \right)^2}, i = 1, 2, 3 \quad (32)$$

$$\bar{\phi}(x) = \frac{1}{3} \sum_{i=1}^3 \phi_i(x) \quad (33)$$

In Figure 7, a sensitivity ranking shows that the variation in porosity is the most influential parameter on the ember combustion, differing from the previous study that activation energy is the dominant parameter.⁴⁶ This is possibly because the glowing combustion of the ember is diffusion-controlled rather than kinetic-controlled due to its high temperature. The heat of reaction ΔH_c and oxygen concentration y_{O_2} play similar secondary roles, while the reaction orders n_{c,O_2} , n_c , heat capacity c_{em} , and particle size d_{p0} have negligible effects on the ember combustion. It should be noted that the wind has double effects on the ember combustion. Moderate wind speed can facilitate the ember combustion by boosting oxygen supply, while violent wind speed will restrain the ember combustion due to significant heat loss to the environment. Therefore, the overall sensitivity coefficient of the wind speed is not as high as

expected. Therefore, modelers should pay more attention to the difference in the physical/thermal properties instead of the kinetics between ember species.

Model validations

To test this computational model, a series of experiments were conducted in a bench-scale flow duct (see Figure 8), which is the same setup used by Urban and colleagues.^{39,47} Laboratory air was flown into the duct which has a 55-cm long test section with a cross-section of 13 cm in width and 8 cm in height. A fuel bed sample holder is located 15 cm from the inlet of the test section such that the upper surface of the fuel bed is flush to the bottom of the test section. The fuel bed sample holder is 15-cm long, 10-cm wide, and 5-cm deep. Visual access is provided through windows on the sides of the test section near the fuel bed holder. Directly over the fuel bed, there is an opening ($13.3 \times 21.0 \text{ cm}^2$) allowing for depositing the embers and for optical access.

The sample holder was filled with a non-reacting “fuel” of sand particles, such that it was flush with the floor of the experimental section. Disk-shaped embers were placed with one face down on the fuel surface such that the center axis of the ember was in line with the center of the exposed fuel surface. It is worth noting that the actual spatial distribution of the ember on the fuel bed varies a lot depending on the wind speed. There were 16 thermocouples (K-type, 0.5-mm diameter) inside the fuel bed to monitor the temperature. The junction sizes for the thermocouples were approximately spherical with a nominal diameter of $1.3 \pm 0.2 \text{ mm}$ (two standard deviations). The thermocouples were placed such that their junctions lay in a plane along the center of the fuel bed (in terms of width) at various locations at regular intervals (shown in the top left graph in Figure 8 by the blue plane). The configuration of the thermocouples is shown in the top right of Figure 8. The uncertainty regarding the locations of the thermocouples is estimated as $\pm 2 \text{ mm}$ in the x , y , and z directions.

The air flow was supplied into the test section at three constant speeds: 1, 2, and 3 m s^{-1} , verified using a hot-wire anemometer. Images of the surface of the fuel and the ember were monitored with an FLIR E60 IR camera, located 75 cm above the fuel bed recording at a rate of 1 Hz. For these images, the IR camera was set to have an emissivity of 0.95 and the external optics transmissivity set to 1. Tests were run for 1000 s (including the heating time). The surface of the ember was imaged using a camera (SONY DSC-RX10 III) calibrated for CP, located 66 cm above the fuel bed, at a rate of 1 Hz until the glowing combustion ceased for the ember.

Embers were produced, measured, and weighed by cutting pieces of a Clear Eastern White Pine (*Pinus strobus*) dowel rod into disks to the desired size. Held by tweezers, each side of the disk embers was exposed to a premixed propane-butane flame for 30 s before being carefully placed on the center of the fuel bed surface. Once the ember was placed on the fuel bed, air flow was supplied into the test section at the three speeds across experiments.

A small set of three tests was performed to examine the characteristic parameters of the ember generated, particularly the temperature, size, and mass. Simultaneous measurements of the three parameters were impractical due to a combination of logistical challenges (i.e., measuring the size or mass of the ember without cooling it or letting it burn). As a result, the sample was imaged first for 4 s using the CP camera (the same amount of time as it takes to

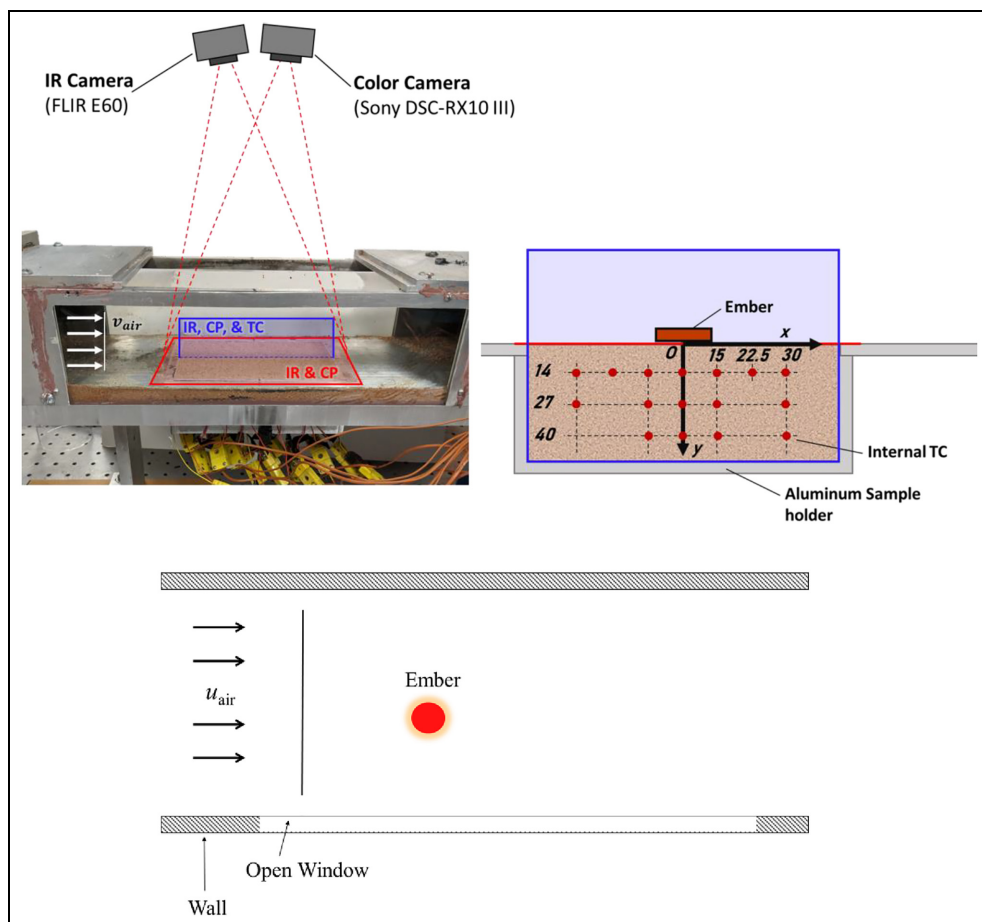


Figure 8. Top left: Flow duct with the fuel bed holder; top right: a plane in which thermocouple junctions (units in mm) are located. Below: sketch of the experimental apparatus (top view).

lay the sample on the fuel bed) before it was quenched in a pan of water in a timely manner. The ember was then removed from the water, placed on a drying rack in a small oven set to 100°C for 4 h, after which point of the size and mass of the ember were measured with a caliper and a scale. It was observed that there was a large decrease in the thickness and mass of the ember after heating, and a small drop of the temperature of the ember after depositing (see Table 6). The ember became black after exposing to a premixed propane-butane flame for 30 s (see Figure S1 in the Supplementary Materials), confirming that it was almost fully charred, and one-step char oxidation is reasonable for simulating its glowing combustion.

Sand was sifted through sieves such that only sand with grain sizes $< 0.5\text{ mm}$ was used. A fuel bed container was filled with the prepared sand with a bulk density of 1390 kg m^{-3} . The moisture content of the sand was measured (dry mass basis) to be 0.13%. The other physical and thermal properties of the sand are listed in Table 7. The temperature of the flow was on average $23.7 \pm 0.7^{\circ}\text{C}$ (2 standard deviations) and the relative humidity was on

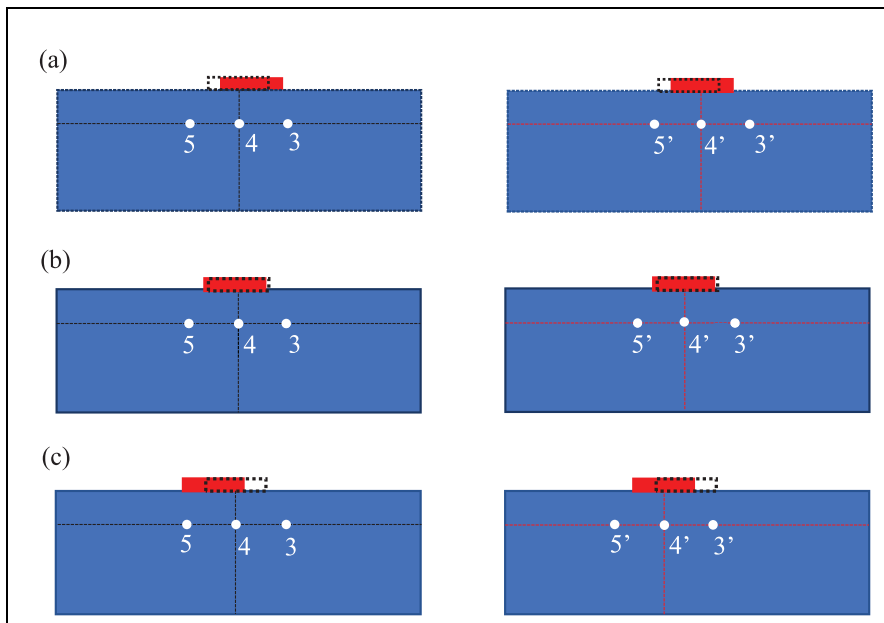
Table 6. Characteristics of the embers used in experiments.

Ember state	Diameter [I]	Thickness [I]	Mass (mg)	Temperature (°C)
Before test ($n = 12$)*	25.47 ± 0.09	8.09 ± 0.15	1983 ± 33	24.84 ± 0.33
After heating ($n = 3$)*	25.02 ± 0.02	5.01 ± 1	179 ± 6	969 ± 71
After depositing ($n = 3$)*	-	-	-	950 ± 20

* n : number of repeated tests.

Table 7. Material properties of the non-reacting sand substrate.

Material	ρ_{sub} (kg m^{-3})	λ_{sub} ($\text{W m}^{-1} \text{K}^{-1}$)	c_{sub} ($\text{J kg}^{-1} \text{K}^{-1}$)	ϕ_{sub} (-)	$K_{sub} \times 10^{-10}$ (m^2)	ε_{sub} (-)
Sand	1390	0.25	800	0.42	2.75	0.9

**Figure 9.** Schematic of the ideal and actual locations of the ember on the sand surface: (a) Test 1, (b) Test 2, and (c) Test 3 under $u_0 = 1 \text{ m s}^{-1}$.

average $17.9 \pm 1.0\%$ (2 standard deviations) for these experiments. The average temperature and relative humidity of the laboratory were on average $24.8 \pm 0.7^\circ\text{C}$ and $38.9 \pm 2.2\%$, respectively.

Owing to the effects of the wind, the ember placed is usually slightly off from the sand center (ideal location). As seen from the left column of Figure 9, the black dashed rectangle

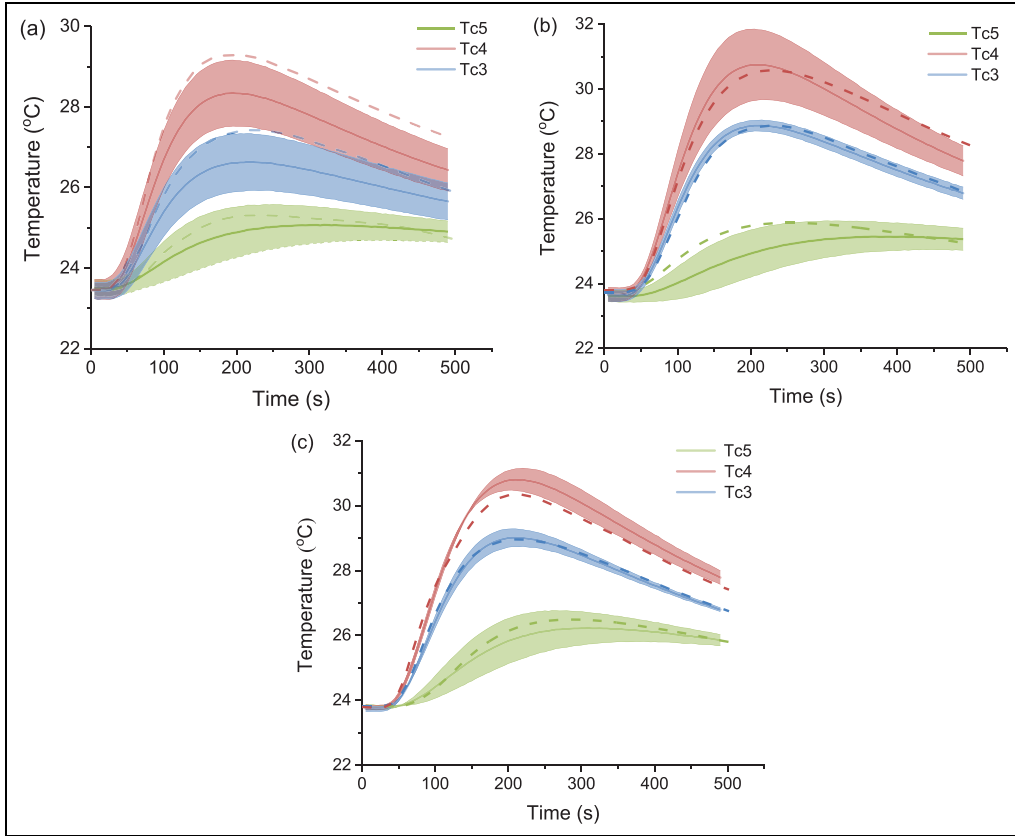


Figure 10. Comparisons between the model and the measured temperatures inside the sand bed at flow speed of (a) $u_0 = 1 \text{ m s}^{-1}$; (b) $u_0 = 2 \text{ m s}^{-1}$; and (c) $u_0 = 3 \text{ m s}^{-1}$. Model: dashed lines; Experiments: solid lines with shaded area (standard error in three repeated experiments).

is the ideal initial location of the ember, while the solid red rectangle is the actual location of the ember. Thermocouple 4 (Tc4) is located -1.4 cm below the bottom center of black-dashed rectangle, Tc3 and Tc5 are $\pm 1.5 \text{ cm}$ away from Tc4, respectively. The actual locations of the ember varied significantly within repeated tests. For a given air velocity, averaging a certain thermocouple temperature within repeated experiments will cause large standard error due to the varied location of ember on the fuel bed. As a result, for each repeated experiments, temperature interpolation at $y = -1.4 \text{ cm}$ (point 4,' see the right column in Figure 9) below the bottom center of the actual location of the ember (solid red rectangle zone in the figure) was measured and used. Temperature interpolation at points 3,' 5,' which are $\pm 1.5 \text{ cm}$ away from point 4,' was also measured and recorded.

The interpolated temperature at points 3,' 4,' and 5,' which stayed symmetrically below the actual location of the ember was averaged from the repeated three experiments. The in-depth temperature distribution below the ember is shown in Figure 10. The shaded area represents the standard error, and the solid lines represent the mean temperature at each point. The comparisons in Figure 10 show a good agreement between the model (dashed lines) and

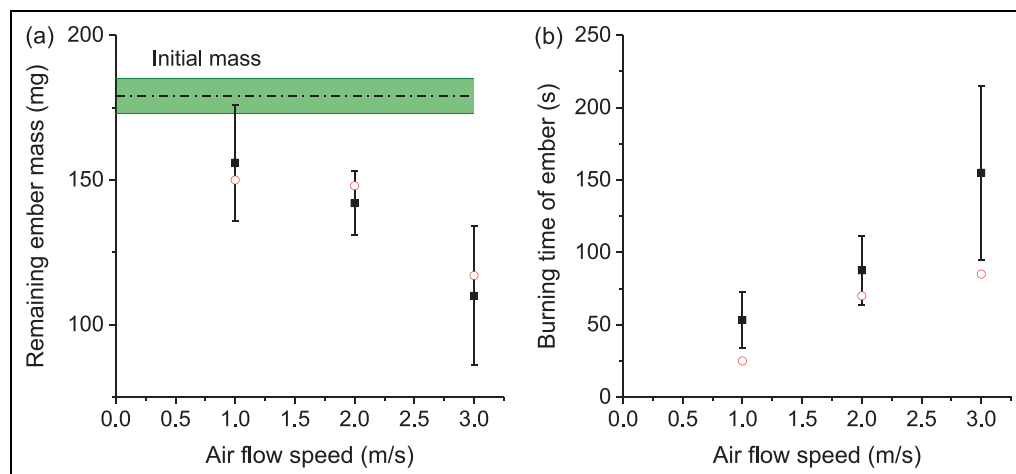


Figure 11. Comparisons of (a) remaining ember mass and (b) glowing time of ember at different air flow speeds between the model predictions and the experimental results. Experimental data: solid squares with error bars; model predictions: void circles.

the experiments (solid lines with shaded area), proving that the proposed model in this work can quantitatively predict the heat transfer from a glowing ember to a non-reacting substrate well.

As seen in Figure 11, none of the embers in the experiment burned completely. In all cases, there were 65%–92% of the ember mass remained at the end of experiment, depending on the flow speed. The glowing time was defined as the time after contacting with the fuel bed to when the maximum temperature of the ember fell below 100°C. The burned mass and the glowing time of ember were found to increase with the air flow speed. This finding is consistent with the measurements conducted in the work by Scott et al.⁷ One possible explanation is that higher speeded air flow increases the glowing combustion rate. The underpredicted burning time by the model is most likely due to the model's assumption: no surface cracking of the ember was considered. In the experiments, the ember surface would be cracking, resulting in a larger porosity compared with the model. Therefore, the burning ember mass exceeded the model predictions, leading to a longer burning time. Generally, a fair agreement between modeling and experimental results is obtained in terms of the burned mass and glowing time. It should be recognized that the heat feedback from a reacting substrate will affect the glowing behavior of the ember. Thus, these experiments conducted on a non-reacting substrate should not be simply applied to an actual fuel without consideration of the reactivity of a reacting substrate.

Conclusion

In this study, a 2D computational model was proposed to study the glowing combustion of a porous wooden ember on a non-reacting substrate. A global one-step char oxidation reaction was proved to be appropriate to represent the glowing combustion of the ember. A curved char oxidation frontline, that is, glowing frontline, was predicted in the model. Generally,

the ML of the ember was divided into three stages: I. Stage with sharp-drop MLR with a small shoulder; II. Stable stage; III. Gradual decay stage. A sensitivity ranking showed that the porosity, heat of reaction, and oxygen concentration were the three most influential parameters on the glowing combustion of the ember, possibly due to the fact that the glowing combustion of the ember at high temperature was diffusion-controlled rather than kinetic-controlled. We thus call for that modelers should pay more attention to the difference in the physical/thermal properties instead of the kinetics between ember species. Moreover, the proposed model was compared to the thermal response data of the non-reacting sand substrate when exposed to a hot ember from a series of conducted experiments. A good agreement of the total ember ML and glowing time, and the interior sand temperatures between the model and the experiments manifested that this model can quantitatively predict the heat transfer from a glowing ember to a non-reacting substrate.

This study proposed a model framework to simulate the ember combustion, including the heat and mass transfer between the ember, environment, and the porous fuel bed. Once the chemical kinetics and physical properties of a fuel bed are well known, this model can be extended to model the underlying physics involved in real spot ignition by a wooden ember. Ongoing study is exploring the prediction of the ember-initiated smoldering or flaming limits and the extinction limits of different wildland fuels. More laboratory scale tests of the flammability of different fuel beds and the capability of embers to ignite fuel beds should be conducted in the future to further verify and improve the proposed model. This study first provides a deeper insight into the glowing combustion of a single ember involved in fire spotting ignition, and furthers the understanding of the glowing behavior of embers involved in wildland and WUI fires.

Acknowledgment

The authors thank the NIST fire research group and NIST WUI group for fruitful discussions.


Declaration of conflicting interests


The author(s) declared no potential conflicts of interest with respect to the research, authorship, and/or publication of this article.

Funding

The author(s) disclosed receipt of the following financial support for the research, authorship, and/or publication of this article: This research was supported by the National Natural Science Foundation of China (grant nos. 52306158 and 52106184), Natural Science Foundation of Sichuan Province (2023NSFSC0189), Sichuan Students' Innovation and Entrepreneurships Training Program (x202310636260 and x202310636263), and Scientific Research Start-up Fund for High-end Talents (qdf20220307).

ORCID iDs

Jiuling Yang  <https://orcid.org/0000-0002-8799-0275>

James Urban  <https://orcid.org/0000-0002-2476-8212>

Supplemental material

Supplemental material for this article is available online.

References

- Radeloff VC, Hammer RB, Stewart SI, et al. The wildland-urban interface in the United States. *Ecol Appl* 2005; 15(3): 799–805.
- Fernandez-Pello AC. Wildland fire spot ignition by sparks and firebrands. *Fire Safe J* 2017; 91: 2–10.
- Ellis P. Fuelbed ignition potential and bark morphology explain the notoriety of the eucalypt messmate “stringybark” for intense spotting. *Int J Wildland Fire* 2011; 20(7): 897–907.
- Ganteaume A, Lampin-Maillet C, Guijarro M, et al. Spot fires: fuel bed flammability and capability of firebrands to ignite fuel beds. *Int J Wildland Fire* 2009; 18(8): 951–969.
- Manzello SL, Cleary TG, Shields JR, et al. On the ignition of fuel beds by firebrands. *Fire Mater* 2006; 30(1): 77–87.
- Fateev V, Agafontsev M, Volkov S, et al. Determination of smoldering time and thermal characteristics of firebrands under laboratory conditions. *Fire Safe J* 2017; 91: 791–799.
- Scott S, Hadden R, Fereres S, et al. Ignition of combustible fuel beds by embers and heated particles. In: *Fall Technical Meeting Western States Section/Combustion Institute*, University of California, Irvine, CA, 16–17 October 2023, pp. 26–27. Pittsburgh, PA: The Combustion Institute.
- Wang S, Ding P, Lin S, et al. Smoldering and flaming of disc wood particles under external radiation: autoignition and size effect. *Front Mech Eng* 2021; 7: 686638.
- Wang S, Ding P, Lin S, et al. Deformation of wood slice in fire: Interactions between heterogeneous chemistry and thermomechanical stress. *Proc Combust Inst* 2021; 38(3): 5081–5090.
- Woycheese J. Wooden disk combustion for spot fire spread. In: *The ninth international fire science and engineering conference (INTERFLAM)*, Edinburgh, 17–19 September 2001. London: Interscience Communication.
- Zhang Z, Ding P, Wang S, et al. Smoldering-to-flaming transition on wood induced by glowing char cracks and cross wind. *Fuel* 2023; 352: 129091.
- Manzello SL, Park S-H and Cleary TG. Investigation on the ability of glowing firebrands deposited within crevices to ignite common building materials. *Fire Safe J* 2009; 44(6): 894–900.
- Hakes RS, Salehizadeh H, Weston-Dawkes MJ, et al. Thermal characterization of firebrand piles. *Fire Safe J* 2019; 104: 34–42.
- Salehizadeh H. *Critical ignition conditions of structural materials by cylindrical firebrands*. Master Thesis, University of Maryland, College Park, MD, 2019.
- Tao Z, Bathras B, Kwon B, et al. Effect of firebrand size and geometry on heating from a smoldering pile under wind. *Fire Safe J* 2021; 120: 103031.
- Bearinger ED, Hodges JL, Yang F, et al. Localized heat transfer from firebrands to surfaces. *Fire Safe J* 2021; 120: 103037.
- Urban JL, Vicariotto M, Dunn-Rankin D, et al. Temperature measurement of glowing embers with color pyrometry. *Fire Tech* 2019; 55: 1013–1026.
- Nazare S, Leventon I and Davis R. Ignitability of structural wood products exposed to embers during wildland fires: a review of literature. *NIST Technical Note* 2021; 2153.
- Abul-huda YM. Development of a spatially resolved optical technique for measuring heat flux and thermal footprint of firebrand piles. *NIST Technical Note* 2019; 205228.
- Ju X, Conkling M, Hajilou M, et al. Laboratory quantification of firebrand generation from WUI fuels for model development. *Fire Safe J* 2023; 141: 103921.
- Manzello SL and Suzuki S. The new and improved NIST Dragon’s LAIR (Lofting and Ignition Research) facility. *Fire Mater* 2012; 36(8): 623–635.
- Wadhvani R, Sullivan C, Wickramasinghe A, et al. A review of firebrand studies on generation and transport. *Fire Safe J* 2022; 134: 103674.
- Lautenberger C and Fernandez-Pello A. Spotting ignition of fuel beds by firebrands. *WIT Trans Model Simul* 2009; 48: 603–612.
- Warey A. Influence of thermal contact on heat transfer from glowing firebrands. *Case Stud Thermal Eng* 2018; 12: 301–311.
- Lin S, Wang S and Huang X. Modeling smoldering ignition by an irradiation spot. *Fire Safe J* 2022; 134: 103708.
- Santamaria S, Kempná K, Thomas JC, et al. Investigation of structural wood ignition by firebrand accumulation. In: *First International Conference on Structures Safety Under Fire Blast*, Glasgow, 17 September 2015. Hefei, China: University of Science and Technology of China.
- Magnaterra M, Fusco J, Ochoa J, et al. Kinetic study of the reaction of different hardwood sawdust chars with oxygen. Chemical and structural characterization of the samples. In: Bridgewater AV (ed.) *Advances in Thermochemical Biomass Conversion*. New York: Springer, 1993, pp. 116–130.
- Boonmee N and Quintiere J. Glowing ignition of wood: the onset of surface combustion. *Proc Combust Inst* 2005; 30(2): 2303–2310.
- Song Z. Modelling oxygen-limited and self-sustained smoldering propagation: Underground coal fires driven by thermal buoyancy. *Combust Flame* 2022; 245: 112382.
- Saidi M, Hajaligol M, Mhaisekar A, et al. A 3D modeling of static and forward smoldering combustion in a packed bed of materials. *Appl Math Model* 2007; 31(9): 1970–1996.
- Van Kuijk H, Van Oijen J, Bastiaans R, et al. Reverse combustion: Kinetically controlled and mass transfer controlled conversion front structures. *Combust Flame* 2008; 153(3): 417–433.
- Janse AM, de Jonge HG, Prins W, et al. Combustion kinetics of char obtained by flash pyrolysis of pine wood. *Ind Eng Chem Res* 1998; 37(10): 3909–3918.
- Anca-Couce A, Zobel N, Berger A, et al. Smoldering of pine wood: Kinetics and reaction heats. *Combust Flame* 2012; 159(4): 1708–1719.
- Manzello SL, Cleary TG, Shields JR, et al. Ignition of mulch and grasses by firebrands in wildland-urban interface fires. *Int J Wildland Fire* 2006; 15(3): 427–431.
- Lautenberger C and Fernandez-Pello C. Generalized pyrolysis model for combustible solids. *Fire Safe J* 2009; 44(6): 819–839.
- Ragland K, Aerts D and Baker A. Properties of wood for combustion analysis. *Bioresource Tech* 1991; 37(2): 161–168.
- Janssens M. Thermo-physical properties for wood pyrolysis models. In: *Pacific Timber Engineering Conference*, Gold Coast, QLD, Australia, 11–15 July 1994. Canberra, ACT, Australia: National Library of Australia.

38. Groenli MG. *A theoretical and experimental study of the thermal degradation of biomass*. Ph.D. Thesis, The Norwegian University of Science and Technology, Trondheim, 1996.
39. Urban JL, Zak CD, Song J, et al. Smoldering spot ignition of natural fuels by a hot metal particle. *Proc Combust Inst* 2017; 36(2): 3211–3218.
40. Di Blasi C. Processes of flames spreading over the surface of charring fuels: effects of the solid thickness. *Combust Flame* 1994; 97(2): 225–239.
41. Yovanovich M. New contact and gap conductance correlations for conforming rough surfaces. In: *AIAA 16th thermophysics conference*, Palo Alto, CA, 23–25 June 1982 (AIAA Paper No. 81-1164). Reston, VA: AIAA.
42. Huang X, Restuccia F, Gramola M, et al. Experimental study of the formation and collapse of an overhang in the lateral spread of smoldering peat fires. *Combust Flame* 2016; 168: 393–402.
43. Yang J, Liu N, Chen H, et al. Effects of atmospheric oxygen on horizontal peat smoldering fires: Experimental and numerical study. *Proc Combust Inst* 2019; 37(3): 4063–4071.
44. Yang J, Wang S and Chen H. Effect of interface thermal resistance on ignition of reactive material by a hot particle. *Int J Heat Mass Trans* 2016; 97: 146–156.
45. Hamby DM. A review of techniques for parameter sensitivity analysis of environmental models. *Environ Monit Assess* 1994; 32: 135–154.
46. Yuan H, Restuccia F, Richter F, et al. A computational model to simulate self-heating ignition across scales, configurations, and coal origins. *Fuel* 2019; 236: 1100–1109.
47. Urban JL, Zak CD and Fernandez-Pello C. Cellulose spot fire ignition by hot metal particles. *Proc Combust Inst* 2015; 35(3): 2707–2714.

Appendix

Notation

Letters		Greek symbols	
<i>A</i>	pre-exponential factor (s^{-1})	α	mass conversion (–)
<i>c</i>	specific heat capacity ($\text{J kg}^{-1} \text{K}^{-1}$)	δ	asperities average height
<i>D</i>	diffusivity ($\text{m}^2 \text{s}^{-1}$)	ε	Emissivity
<i>E</i>	activation energy (kJ mol^{-1})	Γ	Boundaries
F	volume force (N m^{-3})	ϕ	Porosity
g	gravitational acceleration (m s^{-2})	λ	thermal conductivity ($\text{W m}^{-1} \text{K}^{-1}$)
<i>h</i>	conductance	μ	dynamic viscosity ($\text{kg m}^{-1} \text{s}^{-1}$)
<i>H</i>	micro-hardness	θ	asperities average slope
ΔH	heat of reaction (J g^{-1})	ρ	density (kg m^{-3})
<i>K</i>	permeability (m^2)	σ	Stefan–Boltzmann constant ($\text{W m}^{-2} \text{K}^{-4}$)
<i>m</i>	mass (kg)	ν	mass yield
<i>M</i>	molecular mass (g mol^{-1})	ω''	reaction rate ($\text{kg m}^{-3} \text{s}^{-1}$)
<i>ML</i>	normalized mass loss (–)	Subscripts	
<i>MLR</i>	mass loss rate (–)	0	Initial
<i>n</i>	reaction order	<i>a</i>	Ash
<i>p</i>	pressure (Pa)	<i>c/co</i>	char /char oxidation
Q''	heat flux (W m^{-2})	<i>d/du</i>	downside/upside
<i>R</i>	universal gas constant ($\text{J mol}^{-1} \text{K}^{-1}$)	<i>em/eff</i>	ember/effective
<i>T</i>	temperature ($^{\circ}\text{C}$)	<i>ff</i>	free flow
u	velocity vector (m s^{-1})	<i>g</i>	gas phase
<i>x</i>	<i>x</i> coordinate (cm)/ volume fraction	<i>j</i>	gas species
<i>y</i>	<i>y</i> coordinate (cm)/mass fraction	<i>r</i>	radiative
<i>Y</i>	mean separation thickness	<i>sub</i>	substrate

Author biographies

Jiuling Yang, PhD, is a full-time lecturer at Sichuan Normal University, Chengdu, P.R. China. Yang's research areas include pyrolysis kinetics, smoldering mechanisms and spot ignition.

Xiaofeng Peng received a master's degree from Sichuan Normal University, Chengdu, P.R. China. Peng's research areas include spot ignition and computational modelling.

James Urban, PhD, is an Assistant Professor at Worcester Polytechnic Institute, Worcester, MA, US. His research interests include firebrands, compartment fires and WUI fuel flammability.

Wei Huang received his master's from Sichuan Normal University, Chengdu, P.R. China. His research interests include smoldering fires and computational modelling.

Haoliang Wang received his master's from Sichuan Normal University, Chengdu, P.R. China. His research interests include pyrolysis kinetics and smoldering fires.

Shaojia Wang is an undergraduate from Sichuan Normal University, Chengdu, P.R. China. His research interests include firebrands and spot ignition.

Yuqi Hu, PhD, is an Assistant Researcher at the Sichuan Fire Research Institute of the Ministry of Emergency Management of China, Chengdu, P.R. China. His research interests include smoldering fires and forest fire emissions.